

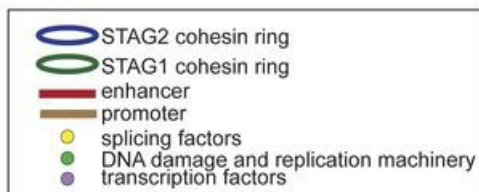
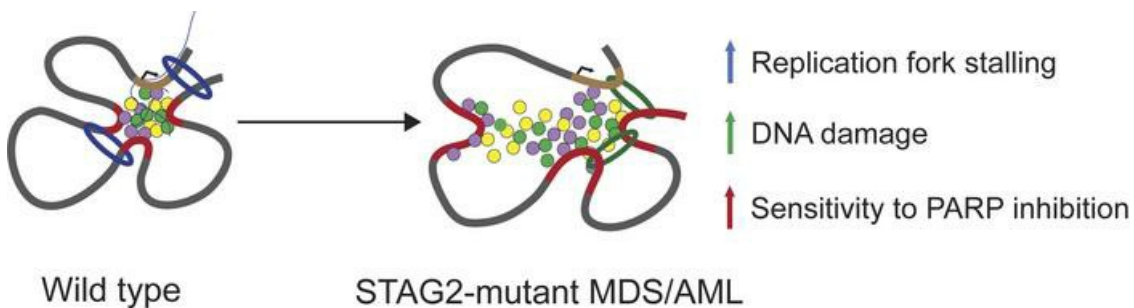
Cohesin mutations alter DNA damage repair and chromatin structure and create therapeutic vulnerabilities in MDS/AML

Zuzana Tothova, ... , Job Dekker, Benjamin L. Ebert

JCI Insight. 2020. <https://doi.org/10.1172/jci.insight.142149>.

Research In-Press Preview Hematology Oncology

Graphical abstract



Find the latest version:

<https://jci.me/142149/pdf>



**Cohesin mutations alter DNA damage repair and chromatin structure and create
therapeutic vulnerabilities in MDS/AML**

Zuzana Tothova^{1,2*}, Anne-Laure Valton³, Rebecca A. Gorelov², Mounica Vallurupalli^{1,2}, John M. Krill-Burger², Amie Holmes⁴, Catherine C. Landers², J. Erika Haydu², Edyta Malolepsza², Christina Hartigan², Melanie Donahue², Katerina D. Popova², Sebastian Koochaki¹, Sergey V. Venev³, Jeanne Rivera⁵, Edwin Chen⁵, Kasper Lage², Monica Schenone², Alan D. D'Andrea⁴, Steven A. Carr², Elizabeth A. Morgan⁶, Job Dekker^{3,7}, Benjamin L. Ebert^{1,2,7*}

¹Dana-Farber Cancer Institute, Department of Medical Oncology, Boston, MA, 02115, USA

²Broad Institute, Cancer Program, Cambridge, MA, 02142, USA

³University of Massachusetts Medical School, Program in Systems Biology, Department of Biochemistry and Molecular Pharmacology, Worcester, MA 01605, USA

⁴Dana-Farber Cancer Institute, Department of Radiation Oncology, Boston, MA, 02115, USA

⁵University of Leeds, Faculty of Biological Sciences, Leeds, United Kingdom

⁶Brigham and Women's Hospital, Department of Pathology, Boston, MA, 02115, USA

⁷Howard Hughes Medical Institute, Chevy Chase, MD, 20815, USA

*Corresponding authors: benjamin_ebert@dfci.harvard.edu, zuzana_tothova@dfci.harvard.edu;
Dana-Farber Cancer Institute, 450 Brookline Avenue, Boston, MA 02215

The authors have declared that no conflict of interest exists.

SUMMARY: We developed models of cohesin-mutant MDS and AML and demonstrated a shift from STAG2- to STAG1-cohesin complexes, increased DNA damage and sensitivity to PARP inhibition.

ABSTRACT

The cohesin complex plays an essential role in chromosome maintenance and transcriptional regulation. Recurrent somatic mutations in the cohesin complex are frequent genetic drivers in cancer including myelodysplastic syndromes (MDS) and acute myeloid leukemia (AML). Here, using genetic dependency screens of *STAG2*-mutant AML, we identified DNA damage repair and replication as genetic dependencies in cohesin-mutant cells. We demonstrated increased levels of DNA damage and sensitivity of cohesin-mutant cells to PARP inhibition. We developed a mouse model of MDS in which *Stag2* mutations arise as clonal secondary lesions in the background of clonal hematopoiesis driven by *Tet2* mutations, and demonstrated selective depletion of cohesin-mutant cells with PARP inhibition *in vivo*. Finally, we demonstrated a shift from STAG2- to STAG1-containing cohesin complexes in cohesin-mutant cells, which is associated with longer DNA loop extrusion, more intermixing of chromatin compartments, and increased interaction with PARP and RPA proteins. Our findings inform the biology and therapeutic opportunities for cohesin-mutant malignancies.

INTRODUCTION

The cohesin complex is a multimeric protein complex that forms a ring structure around DNA molecules and plays multiple key roles in spatial organization of eukaryotic genomes. Cohesin proteins are involved in several essential cellular functions, including sister chromatid cohesion, chromatin loop organization, transcriptional activation, and DNA replication and damage repair, among others (reviewed in(1)). More recently, the cohesin complex was identified as one of the most frequently mutated protein complexes in cancer, including myeloid malignancies, glioblastoma, breast cancer, bladder cancer and Ewing sarcoma(2, 3). The mechanisms by which cohesin mutations cause cellular transformation are unknown, and currently no therapies are known to exhibit selective efficacy in cohesin-mutant cancers.

Myelodysplastic syndromes (MDS) and acute myeloid leukemia (AML) are clonal diseases of mutated hematopoietic stem and progenitor cells (HSPC) characterized by abnormal differentiation and proliferation caused by somatic mutations in genes encoding transcription factors, epigenetic regulators, chromatin modifiers and splicing factors(4, 5). The core components of the cohesin complex *STAG2*, *SMC1*, *SMC3*, *RAD21*, as well as its modulators *PDS5* and *NIPBL*, are collectively mutated in 13% of patients with *de novo* AML, 21% of patients with secondary AML, and 11% of patients with MDS, where they are associated with poor overall survival (5-10). Mutations in the cohesin genes are nearly always mutually exclusive, heterozygous, predicted loss-of-function (LOF) lesions, which are thought to be acquired early during the progression from clonal hematopoiesis of indeterminate prognosis (CHIP) to MDS (4, 11). Targeted inactivation of *Smc3* or *Stag2*, and overexpression of mutant cohesin genes in wild type mouse and human HSPC has been previously studied(12-15) but no cohesin-mutant models currently exist that recapitulate the natural evolution of cohesin-mutant myeloid disease in the context of clonal hematopoiesis.

Two different cohesin complexes are known to co-occur in somatic vertebrate cells, each containing the core components *SMC1A*, *SMC3*, and *RAD21*, and alternatively including *STAG2* or the less abundant *STAG1*(16). *STAG2*- and *STAG1*- complexes associate with centromeres and telomeres, respectively, but their sister chromatid cohesion-independent functional differences are not fully understood(1). *STAG2* mutations account for over 85% of cohesin mutations in MDS, whereas *STAG1* is rarely mutated in MDS or AML(6, 7, 10, 17). The mechanism underlying clonal expansion of these driver mutations is unlikely related to defects in

sister chromatid cohesion given lack of association between *STAG2* mutations and complex karyotype and aneuploidy(10, 18). *STAG1*- versus *STAG2*- containing complexes have been recently shown to differentially contribute to chromatin organization, facilitating longer loops at topologically associating domain (TAD) boundaries and shorter more transient nested enhancer-promoter contacts, respectively(19-22). Furthermore, *Stag2/Runx1* deficiency has been shown to disrupt enhancer-promoter looping and effect transcriptional pausing leading to selective gene dysregulation(22).

We sought to determine the effects of *STAG2* mutations observed in patients on the cohesin complex composition and genetic dependencies, with the goal of understanding the mechanisms by which these mutations contribute to cellular transformation and how cohesin-mutant malignancies could be therapeutically targeted.

RESULTS

Genetic synthetic vulnerabilities in *STAG2*-mutant cells

To study the cellular consequences of cohesin mutations in myeloid malignancies, we used CRISPR-Cas9 to engineer a spectrum of predicted LOF *STAG2*, *SMC3* and *RAD21* mutations identified in patients in AML cell lines wild type for all cohesin subunits and modulators. The different mutants largely phenocopy each other and are consistent with loss of function of *STAG2* or haploinsufficiency of *SMC3* or *RAD21* (Supplementary Fig. S1A-G, Methods). We first focused on *STAG2*, the most frequently mutated subunit of the cohesin complex and hypothesized that different *STAG2* mutations would be associated with mutant-specific genetic dependencies.

We performed genome-scale CRISPR-Cas9 screens in 6 wild type and 5 *STAG2*-mutant U937 cell lines representing different *STAG2* mutations using the Avana sgRNA library, which targets a total of 20,000 protein-coding genes with four unique sgRNAs per gene and includes 1000 non-targeting sgRNA controls(23). We observed that *STAG2*-mutant cells were strongly dependent on *STAG1*, as has been recently reported in the context of bladder cancer and Ewing sarcoma cell lines(24, 25) (Fig. 1A, Supplementary Fig. S2A). Since both *STAG1*- and *STAG2*-containing cohesin complexes participate in sister chromatid cohesion, we examined whether loss of *STAG1* in *STAG2*-deficient cells would lead to aberrant sister chromatid cohesion. We found that loss of both *STAG1* and *STAG2*, but not loss of either one alone, led to sister chromatid cohesion defects as assessed by premature centromere separation and railroad chromosomes (Fig. 1B), providing a mechanistic basis for the synthetic lethality of *STAG1* and *STAG2*. The absence of sister chromatid cohesion defects in cells harboring loss of *STAG2* alone is in agreement with lack of aneuploidy or complex karyotype in patients with *STAG2*-mutant MDS and AML(5, 10, 26), as well as previous studies in yeast suggesting that sister chromatid cohesion is unaffected with up to 87% loss of cohesin levels(27). Therefore, *STAG2*-mutant cells are dependent on the presence of *STAG1* and do not have overt sister chromatid cohesion defects unless accompanied by a simultaneous loss of *STAG1*.

In addition to *STAG1*, we identified preferential dependency of *STAG2*-mutant cells on multiple components of the DNA damage repair and replication machinery (Fig. 1A), as well as lineage-defining transcription factors, and genes involved in mRNA processing (Supplementary Table S1). Of note, we identified multiple members of the base excision repair (PARP1), homologous recombination (BRIP1, RAD51B, RAD51C, RAD54L2, XRCC2, XRCC3, PARP1), mismatch

repair machinery (MSH2, POLD3, EXO1) and DNA replication (RPA2, POLD3) as specific synthetic vulnerabilities of *STAG2*-mutant cells (Fig. 1A). Therefore, we observed differential dependency of *STAG2*-mutant cells on DNA damage repair and replication-associated pathways.

Altered cohesin complex composition and interactome in *STAG2*-mutant cells

Having demonstrated that *STAG2* mutations lead to genetic dependencies on *STAG1* and DNA damage repair and replication, we hypothesized that these cohesin-dependent vulnerabilities could be associated with mutant-specific protein complex alterations. To examine the effect of *STAG2* loss on the composition of the cohesin complex, we employed immunoprecipitation using an antibody against the core cohesin ring subunit *SMC1A* followed by quantitative mass spectrometry (IP-MS) (Supplementary Fig. S2B). In wild type cells, we detected all members of the cohesin complex, including direct binding partners *SMC3* and *RAD21*, as well as indirect binding partners *STAG1*, *STAG2* and *PDS5B* (Supplementary Fig. S2C and S2D, Supplementary Table S2a). In comparison, examination of *STAG2*-mutant clones revealed *STAG1* to be among the most enriched proteins preferentially incorporated into the cohesin complex in cohesin-mutant cells (hereafter referred to as *STAG1*-cohesin complex for simplicity) (Fig. 1C, Supplementary Table S2b). We validated this switch to *STAG1*-containing complexes in *STAG2*-mutant cells using immunoprecipitation followed by western blotting (IP-WB) (Supplementary Fig. S2E). A switch from *STAG2* to *STAG1*-cohesin complexes was consistent with the dependency of *STAG2*-mutant cells on *STAG1* (Fig. 1A). Unexpectedly, we also observed increased incorporation of *STAG1* into cohesin complexes in cells with heterozygous mutation of a non-*STAG1/2* paralog cohesin subunit, *SMC3* (Supplementary Fig. S2F and S2G, Supplementary Table S2c). These studies provide evidence that mutation of either *STAG2* or *SMC3* causes a shift to *STAG1*-containing cohesin complexes.

We next examined whether the shift from *STAG2*- to *STAG1*-containing cohesin complexes is associated with additional changes in its interactome that could explain the genetic dependencies that we had observed. We observed a significant increase in the interaction of the *STAG1*-cohesin complex with proteins involved in DNA replication and DNA damage repair (e.g. *PARP1*, *RPA1-3*; $p=0.024$) (Fig. 1C), transcription factors and splicing proteins (Supplementary Table S2b). Similarly, we observed changes in the interaction of the *STAG1*-cohesin complex with the DNA damage repair, replication, and splicing machinery in *SMC3*-mutant cells (Supplementary Fig. S2F), suggesting that mutations affecting different cohesin subunits may affect the cohesin complex structure and interactome concordantly. These findings demonstrate a high concordance

between the cellular processes highlighted by IP-MS experiments and genetic dependency screens in cohesin-mutant cells, especially as it relates to DNA replication and damage repair.

Stalled replication forks and accumulation of dsDNA breaks in *STAG2*-mutant cells

Having found that *STAG2* mutations were associated with a genetic dependency on components of the DNA replication and damage repair pathways, and altered interaction of these proteins with the cohesin complex, we examined whether cells bearing *STAG2* mutations accumulate DNA damage. Cohesin has been shown to organize chromatin loops at DNA replication factories in order to mediate replication stress tolerance and restart stalled replication forks(28-32). Since aberrant replication forks could serve as a potential source of DNA damage in cohesin-mutant cells, we investigated DNA replication fork processivity using a DNA fiber assay(33). Loss of *STAG2* was associated with an increase in the number of stalled replication forks (6% in wild type cells versus 25% in *STAG2*-mutant cells, $p < 0.05$) and a tendency to lose replication origin firing (Fig. 1D). Furthermore, we observed significant replication fork asymmetry and a 27% decrease in the replication fork rate in *STAG2*-mutant cells (Supplementary Fig. S3A-B), both of which are consistent with replication fork slowing and stalling. Therefore, *STAG2* mutations are associated with abnormal replication fork processivity and stalling, a phenomenon that may be due to aberrant spatial arrangement of replication origins and/or ineffective restarting of replication forks in the absence of a normal cohesin complex.

Stalled replication forks can lead to DNA damage, including dsDNA breaks if inappropriately resolved. The cohesin complex has been previously implicated in dsDNA break repair and intra-S and G2M checkpoint(34). *STAG1*- versus *STAG2*- containing cohesin complexes have been shown to affect repair pathway choice, with *STAG2*-cohesin complex being preferentially involved in sister chromatid homologous recombination repair(35). We therefore examined γ -H2Ax accumulation using immunoblotting as an indicator of dsDNA breaks. We observed accumulation of γ -H2Ax staining under homeostatic conditions across all *STAG2*-mutant cell lines (Fig. 1E). This was associated with activation of the ATR and ATM DNA damage checkpoints as assessed by phosphorylation of ATM and ATR proteins (Fig. 1F), even in the absence of mitomycin C treatment, which is predicted to induce DNA damage by blocking both replication and transcription. These data therefore indicate that one of the functional consequences of *STAG1*-cohesin complexes is aberrant DNA damage repair and increased genomic instability.

STAG2*-mutant cells are sensitive to PARP inhibition *in vitro* and *in vivo

We next addressed whether altered DNA damage response in *STAG2*-mutant cells creates a vulnerability that can be exploited therapeutically. In our CRISPR screen for genetic dependencies, we found *STAG2*-mutant cells to have a genetic dependency on *PARP1* (Fig. 1A, $p=0.006$); and in our IP-MS experiments, we found an increased association of *PARP1* with the cohesin complex in *STAG2*-mutant cells (Fig. 1C, $\log_2FC=1.03$). Furthermore, genetic screens in *S.cerevisiae* and *C. elegans* had previously identified synthetic lethality interactions between replication fork mediators, including *PARP* (poly (ADP-ribose) polymerase) genes, and mutant cohesin(36). We therefore tested sensitivity of *STAG2*-mutant cells to *PARP* inhibition. *PARP* inhibitors, including talazoparib, inhibit *PARP* catalytic activity and trap *PARP* at the sites of DNA damage, rendering cells that are dependent on non-homologous end joining repair of dsDNA breaks particularly sensitive to these agents. Treatment with talazoparib resulted in ~70-fold increased sensitivity of *STAG2*-mutant cells as compared to wild type cells (Fig. 2A). In addition, *STAG2*-mutant cells were outcompeted by wild type cells in the presence of talazoparib (Fig. 2B). We also sought to determine whether mutations in other components of the cohesin complex result in a similar dependency on *PARP* inhibition. We found that heterozygous inactivation of *SMC3* or *RAD21* was associated with increased sensitivity to *PARP* inhibition to a similar extent as *STAG2* mutations in U937 and K562 cells (Fig. 2C, Supplementary Fig. S3C), suggesting that all core cohesin complex mutations we have tested may act as biomarkers of response to *PARP* inhibition.

We reproduced this effect in xenograft animals injected with individual or competitive mixtures of wild type and *STAG2*-mutant AML cells and observed a genotype-specific effect of talazoparib on *STAG2*-mutant cells (Fig. 2D-E). Finally, in order to examine whether response to *PARP* inhibition in primary human leukemia cells is *STAG2* mutation dependent, we treated *STAG2*-mutant and wild type primary AML patient samples with talazoparib and noted a dose and genotype-dependent sensitivity to the drug (Supplementary Fig. S3D). Cumulatively, these studies indicate that cohesin complex mutations result in increased association of DNA repair factors with mutant *STAG1*-containing cohesin complexes, impaired DNA damage repair and increased sensitivity to *PARP* inhibitors.

Development of cohesin-mutant mouse models of MDS and AML

In order to extend our observations made in AML cell lines to primary models of *STAG2*-mutant myeloid disease, we developed a syngeneic mouse model in which *Stag2* mutations arise as secondary lesions in the background of clonal hematopoiesis driven by *Tet2* mutations, as is seen

in the development of human MDS (4) (Fig. 3A). Hematopoietic stem and progenitor cells (Lineage-, Sca1+, c-Kit+ cells) harvested from Mx1-Cre; Cas9 heterozygous C57BL.6 mice were transduced with sgRNA targeting *Tet2* or non-targeting sgRNA (NTG) and transplanted into lethally irradiated SJL recipient mice. Engraftment and clonal expansion of *Tet2*-mutant cells were confirmed by fluorescent protein reporter expression and next-generation sequencing (37), and were not associated with an overt phenotype (Fig. 3B). Next, c-Kit enriched bone marrow cells from mice with *Tet2* mutations (*Tet2* indel fraction 0.62) were transduced with sgRNAs targeting *Stag2* or NTG and transplanted into secondary recipient mice. Cells with *Tet2/Stag2* genetic editing expanded relative to *Tet2/NTG* cells by 2 months post-transplantation (Fig. 3C). In contrast to *Tet2*-only mutant mice, *Tet2/Stag2*-mutant mice developed leukocytosis, absolute monocytosis, anemia, and thrombocytopenia (Fig. 3D).

Morphologic evaluation of *Tet2/Stag2* bone marrow revealed fewer megakaryocytes and increased hemophagocytosis consistent with macrophage activation in comparison to *Tet2*-only mutant mice (Fig. 3E). NGS confirmed predicted loss of function frameshift mutations in *Tet2* and *Stag2* (mean *Tet2* indel fraction 0.80 in *Tet2/NTG* mice; mean *Tet2* and *Stag2* indel fractions 0.64 and 0.63, respectively, in *Tet2/Stag2* mice). In concordance with our AML cell line data, *Tet2/Stag2*-mutant bone marrow cells exhibited higher levels of dsDNA breaks and increased sensitivity to treatment with talazoparib when cultured *in vitro* (Supplementary Fig. S3E-G). *Ex vivo* low dose irradiation of bone marrow cells led to an increase in dsDNA breaks in *Tet2/NTG* cells treated with vehicle but did not appreciably increase already elevated levels of dsDNA breaks in *Tet2/Stag2* or any of the talazoparib treated cells. These studies demonstrate that our CRISPR-Cas9 model with sequential acquisition of *Tet2* and *Stag2* mutations results in aberrant hematopoiesis with *Stag2*-mutant-specific alterations in DNA damage response.

Talazoparib depletes cohesin-mutant clones in *in vivo* models of MDS and AML

Tet2/Stag2 and *Tet2*-mutant clones and the associated hematologic phenotypes were serially transplantable, enabling evaluation of genotype-specific response to the PARP1 inhibitor talazoparib *in vivo*. Forty recipient mice transplanted with *Tet2* or *Tet2/Stag2* mutant bone marrow cells were stratified into treatment groups with talazoparib or vehicle (Fig. 4A). Expression of congenic markers and fluorescent reporters linked to *Tet2* and *Stag2* sgRNA expression were used to monitor mice during 4 weeks of treatment. *Tet2/Stag2*-mutant mice but not *Tet2*-only mutant mice treated with talazoparib demonstrated a significant loss of mutant cells as determined by NGS and flow cytometry (Fig. 4B, Supplementary Fig. S4A). In addition, we observed

normalization of leukocytosis, monocytosis and thrombocytopenia in *Tet2/Stag2* mutant mice treated with talazoparib (Fig. 4C), which was associated with increased numbers of megakaryocytes on blinded review (Fig. 4D, Supplementary Fig. S4B, $p=0.007$).

We next wanted to examine whether response to PARP inhibition is cohesin mutation dependent in primary patient derived leukemia cell xenografts. We developed 2 unique serially transplantable PDX models of *STAG2* and *RAD21*-mutant AML (Fig. 4E, Supplementary Fig. S4C and S4E) and evaluated the efficacy of talazoparib in both models *in vivo*. We noted a decrease in disease burden and increased survival of cohesin-mutant PDX models treated with talazoparib as compared to vehicle (Fig. 4F and 4G, Supplementary Fig. S4D and S4F). Therefore, in both primary mouse HSPC and human AML cells, *STAG2*-mutant cells are selectively sensitive to treatment with talazoparib.

STAG2 loss alters chromatin compartmentalization and looping

In order to understand the impact of the aberrant cohesin complex on chromatin compartmentalization and looping which has been previously linked to DNA replication stress and damage(38), we performed Hi-C(39, 40) in a set of *STAG2*-wild type and knockout AML cell lines. This unbiased genome-wide chromosome conformation analysis enables evaluation of chromatin organization at multiple tiers of genome organization, including compartments, topologically associating domains (TADs) and loops. Compartments are apparent by the plaid pattern of interaction in Hi-C interaction maps (Fig. 5A). Analysis of this pattern is routinely performed by principal component analysis, where PC1 typically captures the positions of compartment domains. The strength of compartmentalization can then be visualized and quantified by re-arranging chromatin interaction maps by ordering loci according to their PC1 value to produce compartmentalization “saddle plots”(41). We observed a global weakening of compartmentalization and spatial segregation of active and inactive chromatin domains in *STAG2*-knockout cells (Fig. 5B), consistent with more intermixing between expression-rich “A compartments” and expression-poor “B compartments” as defined previously(39). Also, the number and location of TAD boundaries, determined by insulation score analysis(42), was largely preserved between *STAG2*-wild type and mutant cells (Supplementary Fig. S5A), but the strength of TAD boundary insulation was globally weakened (Fig. 5C and 5D, Supplementary Fig. S5B).

Finally, we assessed the effects of *STAG2* loss on the strength and size-distribution of positioned loops that are apparent as dots in Hi-C interaction maps and correspond to enriched CTCF-CTCF

interactions at the bases of the loops(43). Visual inspection of the heatmaps revealed stronger dots further away from the diagonal (arrows in Fig. 5E). Genome-wide average loop size and loop density can be estimated by analysis of the relationship between interaction frequency (P) and genomic distance (s) (Supplementary Fig. S5C). Specifically, the position of a local maximum in the derivative of $P(s)$ has been previously shown to represent the average loop size(44). In *STAG2*-wild type cells loops are on average 100-200 kb, while in *STAG2* knockout cells the average loop size is 200-300 kb. In addition, we noted the loop density to be reduced in *STAG2* knockout cells (Fig. 5F).

Combined, these findings show that in the absence of *STAG2*, *STAG1*-containing cohesin complexes extrude larger and somewhat fewer loops. Possibly, *STAG1*-containing cohesin complexes are blocked less efficiently at CTCF sites (resulting in reduced insulation at CTCF sites and TAD boundaries), allowing the loops to more frequently pass CTCF sites and the formation of larger loops. This longer-range extrusion process is also expected to lead to more intermixing of A and B compartments.

***STAG2* loss leads to increased co-localization of cohesin with DNA replication and damage repair proteins**

A unifying hypothesis for genetic and pharmacologic dependencies on DNA replication and damage response is that altered chromatin insulation and compartment structure in cohesin-mutant cells leads to shifts in the physical co-localization of proteins involved in these cellular processes. We addressed this hypothesis using super-resolution microscopy. Staining for SMC1A protein, we identified wild type and mutant cohesin protein complex aggregates as distinct nuclear puncta (Fig. 5G). We observed increased co-localization of the *STAG1*-cohesin complex with PARP1 and RPA1 (Fig. 5G). Therefore, we observed *STAG2* mutant-dependent alterations in the physical co-localization of the cohesin complex with DNA damage, concordant with our previously identified changes in the cohesin interactome and genetic dependencies. Put in context with our Hi-C analysis, we hypothesize that these changes may be driven by increased processivity of the *STAG1*-cohesin complex associated with a loss of TAD boundary insulation and longer loop extrusion.

These findings are consistent with a model in which cohesin complexes in wild type and cohesin-mutant cells, defined by their unique composition have differential ability to maintain chromatin organization as it relates to spatial organization of DNA damage repair machinery. Decreased co-

localization and function of these components in turn creates vulnerabilities that have the potential to be exploited therapeutically in patients with cohesin-mutated malignancies.

DISCUSSION

Our studies establish a role for DNA damage, DNA replication and chromatin architecture in the biology and therapeutic targeting of cohesin-mutant myeloid malignancies. Using genetic screens, IP-MS, chromatin conformation studies and super-resolution microscopy, we demonstrate that the introduction of cohesin mutations results in a switch from STAG2 to STAG1-cohesin complexes and differential cohesin dependence on the DNA damage repair and replication. We observed global spatial chromatin reorganization, including longer loop extrusion, loss of insulation at TAD boundaries and intermixing of compartments, associated with changes in cohesin interaction with DNA replication and damage machinery, which may explain the basis for the genetic dependency we observed. We extended these findings to loss-of-function mutations in other members of the cohesin complex, including *SMC3* and *RAD21*, and identify cohesin mutations as potential biomarkers of response to treatment with PARP inhibitors.

There are currently very limited therapeutic options for patients with MDS and no therapies have been identified with selective activity in cohesin-mutant disease. We found that cohesin mutations cause a 70-fold increased sensitivity to PARP inhibition and are a potential biomarker of PARP inhibitor sensitivity in cohesin-mutant myeloid malignancies. PARP inhibitors are currently approved by the FDA for treatment of breast and ovarian cancer in the context of germline *BRCA* mutations and have been previously tested in a Phase 1 study of unselected patients with advanced hematologic malignancies(45). The effect of talazoparib monotherapy in cohesin-mutated AML or MDS with excess blasts is under investigation in a pilot proof-of-concept study (ClinicalTrials.gov Identifier NCT03974217). *STAG2*- mutant glioblastoma cells have been previously shown to be sensitive to PARP inhibition *in vitro*(31, 46), and cohesin mutations may be potential biomarkers of PARP sensitivity in bladder cancer and Ewing sarcoma, where these mutations are common. In addition, combination treatment of hypomethylating agents and PARP inhibition should be considered given sensitivity of cohesin-mutant MDS and genetically engineered CD34+ cells to hypomethylating agents(9, 47), as well as increased sensitivity of PARP inhibition when administered with low dose hypomethylating agents in preclinical studies(48). Finally, the role of PARP inhibition as a therapeutic strategy may be efficacious in a wider range of myeloid malignancies characterized by DNA damage repair defects, including *IDH1/2*-, *FLT3-ITD*-, splicing factor mutant and AML1-ETO rearranged AML(49).

A number of studies have previously examined the effects of complete cohesin loss on chromatin organization, both in the context of an inducible loss of the essential cohesin subunit RAD21 in human cells and loss of the cohesin-loading factor Nipbl in mice(50, 51). These studies confirmed the essential function of the cohesin complex in formation of topologically associated domains, which is independent of compartment organization. The models used to establish these findings represent a complete loss of cohesin complex, which is not tolerated in human cells, and as a result is not implicated in human disease. Patients with cohesin-mutant myeloid malignancies never present with complete, biallelic inactivation of any cohesin subunit, with the notable exception of STAG2, which has a paralog, STAG1. Complete loss of STAG1 and STAG2 is synthetically lethal in our studies as well in other recent reports(24, 25) and demonstrated in primary mouse hematopoietic stem cells using *Stag2*-conditional knockout mice(15). The models used in our study aimed to recapitulate the extent of cohesin dysfunction that would be observed in human disease, using both engineered cell lines as well as primary mouse models of cohesin-mutant MDS and AML. Cohesin mutations are early but usually not initiating lesions in myeloid malignancies. Our *in vivo* model of cohesin-mutant MDS arising in a setting of *Tet2*-mutant clones recapitulates the sequential acquisition of cohesin mutations in the context of *Tet2*-mutant clonal hematopoiesis and the phenotype observed in patients. The approach we developed is highly adaptable and can be used to not only model different stages of disease progression in hematopoietic malignancies, but also address the question of order of mutation acquisition and questions of necessity versus sufficiency for transformation using different genetic combinations.

Cohesin has been previously shown to organize chromatin loops at DNA replication factories into rosette-like structures, which allows for organized firing of multiple origins of replication and is disrupted with lower levels of cohesin leading to longer loop formation, similar to our observations with STAG2- versus STAG1-cohesin complexes (38). How exactly changes in chromatin organization mediated by the switch from STAG2- to STAG1-containing cohesin complexes in cohesin-mutant cancer cells lead to DNA replication stress and DNA damage repair defects cells remain to be elucidated.

Significant progress has been made in the last two decades in our understanding of the spatial organization of eukaryotic genomes (reviewed in (52)). Acquisition of genetic lesions that affect chromatin architecture are common mechanisms of cellular transformation(53, 54). Our study sheds light on how mutations affecting the cohesin complex alter the biology of mutant MDS and leukemia cells in a manner that creates a specific therapeutic vulnerability to PARP inhibitors.

METHODS

Cell Lines

U937 and K562 cells were obtained from the Broad Institute Cancer Cell Line Encyclopedia where they were authenticated by short tandem repeat (original source of U937 and K562 cells was ATCC). Cells were grown in RPMI (Invitrogen) and supplemented with 10% fetal calf serum (Sigma) and 100u/mL penicillin and 100ug/mL streptomycin (Invitrogen).

Mice

8-10 week old female NSGS mice (NOD-SCID; IL2R γ null; Tg(IL3, CSF2, KITL); strain 013062) and 8-10 week old female SJL mice (B6.SJL-Ptprc; strain 002014) were obtained from The Jackson laboratory. Conditional Cas9 knock-in mice (strain 026175) and Mx1-Cre mice (strain 003556), both obtained from The Jackson laboratory, were bred to generate donors for bone marrow transplantation studies. All mice were housed in a pathogen-free animal facility in microisolator cages and experiments were conducted according to an IACUC approved protocol at the Broad Institute.

Generation of cohesin-mutant single cell clones

U937- and K562-Cas9 expressing cells were first generated by lentiviral transduction with a lentiviral vector pLX-311Cas9 (Addgene #96924). sgRNAs targeting *STAG2*, *SMC3*, *RAD21* or non-targeting sgRNAs were cloned into a minimal backbone plasmid (Addgene #41824) and transfected into U937-Cas9 or K562-Cas9 cells using nucleofection (Lonza, Nucleofector II). GFP+ cells were single cell sorted into 96 well plates and grown up into single cell clones, which were confirmed by DNA sequencing of the targeted locus, as well as Western blotting. Of note, since *STAG2* is an X-linked gene which undergoes normal X-inactivation in females, patients with predicted loss-of-function (LOF) *STAG2* mutations are predicted to lack normal *STAG2* expression. Therefore, in both cases of U937 cells and K562 cells, which both carry two copies of the X chromosome, we screened for presence of homozygous *STAG2* LOF mutations. See Supplemental Methods.

The following sgRNAs targeting human genes were used in this study individually:

STAG2 (exon 4): TCTGGTCCAAACCGAATGAA
STAG2 (A1): AATGTCTTACTGCTCTACAA
STAG2 (A2): CTGAATGTCATCCTCCCGT
STAG1 (G1): GGAATTAGAGGAGCAGGCCG
SMC3 (gRNA 1): GATAAAATGAGACGAGCCC
SMC3 (gRNA 5): GAATATAACCATTTACAATC
RAD21 (gRNA 2): TGTGTTTCGAGTGTAATTTAG
Non-targeting (GC1): GACGGAGGCTAAGCGTCGCAA
Non-targeting (GC3): GATCGTTTCCGCTTAACGGCG

The single cell derived cell lines generated and used in the paper are listed in Supplemental Data Table 3.

CRISPR lentiviral transduction

sgRNAs targeting *STAG2* or *SMC3* were cloned into lentiCRISPRv2 (Addgene #52961) as described (<http://genome-engineering.org/gecko/wp-content/uploads/2013/12/lentiCRISPRv2-and-lentiGuide-oligo-cloning-protocol.pdf>).

Genome-wide CRISPR screening and differential dependency analysis

5 *STAG2*-mutant and 6 *STAG2*-wild type U937 cells expressing Cas9 were infected with the genome-wide human Avana LentiGuide-Puro CRISPR library (Broad Genetic Perturbations Platform), which contains ~75,000 sgRNAs targeting ~19,000 genes and 1000 controls, in two separate experiments, as previously described (23). See Supplemental Methods.

Western blotting, immunoprecipitation and mass spectrometry

Details of Western blotting, immunoprecipitation and immunoprecipitation followed by mass spectrometry performed using iTRAQ and TMT6 labeling are detailed in the Supplemental Methods.

***In vitro* talazoparib treatment and competition assays**

Talazoparib was purchased from Selleck (S7048) and dissolved in DMSO. All drug dose response assays were conducted using CellTiter-Glo luminescent cell viability assay (Promega). Competition experiments were carried out with GFP- and mCherry- labeled cohesin-mutant cells mixed at different ratios, and monitored by flow cytometry. See Supplemental Methods.

DNA fiber assay, Cohesion defect analysis, Super-resolution microscopy

See Supplemental Methods

Bone marrow transplantation assays

C-kit enriched cells isolated from male donors were transduced with the lentiviral constructs containing *Tet2*, *Stag2* or non-targeting (NTG) sgRNA. We specifically used male donors for our experiments since *Stag2* is an X-linked gene and we were interested in modeling loss of *Stag2* expression similar to what has been observed in patients with *STAG2* LOF mutations. Cells were spin-infected with lentivirus in at 37°C for 90 min at 2000rpm, washed twice and injected into animals within 6 hours after transduction.

The following sgRNAs targeting mouse genes were used in the study:

Tet2 sgRNA: TCAGGGGCGATGATGTACAT

Stag2 sgRNA: TAACACACAAAGACAGTACG

Please see Supplemental Methods for additional details of transplantation assays and mouse analysis.

Generation of patient-derived xenograft (PDX) models

PDX#1 AML model was generated from bone marrow mononuclear cells of a patient with *STAG2*-mutant AML, confirmed by Dana-Farber Cancer Institute's Rapid Heme Panel (RHP) sequencing (*STAG2* p.31012* VAF 0.92; *ASXL1* p.G642fs* VAF 0.513; *NRAS* p.G13D VAF 0.426; *RUNX1* p.320* VAF 0.48). PDX#2 AML was generated from a skin lesion of a patient with *RAD21*-mutant AML (*RAD21* p.R586* VAF 0.287; *FLT3* p.D835Y VAF 0.514; *RUNX1* p.Q265 VAF=0.295; *WT1* p.R301fs16* VAF 0.287; *WT1* p.T377fs* VAF 0.278). See Supplemental Methods.

***In vivo* drug treatment**

Two donor *Tet2/Stag2* and two donor *Tet2/NTG* mice were used to generate a cohort of mice for *in vivo* talazoparib experiments. 10 mice per arm were dosed with 0.25mg/kg talazoparib or vehicle in 0.5% methylcellulose once daily by oral gavage. For drug treatment of PDX models, the mice were dosed with 0.25mg/kg talazoparib or vehicle in 0.5% methylcellulose (n=9-10 mice/arm for *STAG2*-mutant PDX, n=4 mice/arm for *RAD21*-mutant PDX). See Supplemental Methods.

Indel sequencing analysis. All sequencing analyses were performed on DNA extracted from 1 million murine bone marrow cells using the QIAamp DNA Micro Kit (Qiagen 56304). A sequential PCR was used to amplify the predicted Cas9 cut sites at both the *Tet2* and *Stag2* locus, as previously described, and all primers are listed in the table below (Tothova et al., 2017). Next generation sequencing using the MiSeq desktop sequencer (Illumina) was performed, and 300bp single end reads were used to identify indels. The depth of sequencing was above 10,000 reads for each gene. CRISPR-Seq, a publicly available method on Terra (<https://terra.bio/>), a cloud based genomic analysis platform, was used to detect indels. The pipeline has been previously described (Tothova et al., 2017). Reads were mapped against mouse genome build Mm10.

The following sequencing primers were used:

For mTet2 sgRNA (TCAGGGGCGATGATGTACAT):

FORWARD 5'- Sequencing Primer - Genomic Primer - 3'

ACACTCTTTCCCTACACGACGCTCTTCCGATCT GGTCACCCTCAATAGAGAAGACA

REVERSE 5'- Sequencing Primer – Genomic Primer - 3'

GTGACTGGAGTTCAGACGTGTGCTCTTCCGATCT TGGGCAGCTCTCCTATCCTT

For mStag2 sgRNA(TAACACACAAAGACAGTACG):

FORWARD 5'- Sequencing Primer - Genomic Primer - 3'

ACACTCTTTCCCTACACGACGCTCTTCCGATCTTTGGCTGCATAATAATAGCCTAAAC

REVERSE 5'- Sequencing Primer – Genomic Primer - 3'

GTGACTGGAGTTCAGACGTGTGCTCTTCCGATCT AGTTGATGACTGCTTTGGTAAATG

Hi-C methods and data processing

Hi-C was performed as described previously(40) with some minor modifications. Please see Supplemental Methods for details.

Statistics

A P value less than 0.05 or an adjusted P value/FDR of less than 0.05 were considered significant. Statistical significance of differences in cohesion defects between wildtype and single and double cohesin knockout cells was determined using a one-way ANOVA (Fig. 1B). Statistical significance of enrichment of DNA damage repair and replication proteins was determined using a one-tailed Fisher's exact test (Fig. 1C). Statistical significance of differences in replication fork stalling between wildtype and single and double cohesin knockout cells was determined using a two-tailed unpaired t test (Fig. 1D). Statistical significance of differences in leukemia burden between mice treated with talazoprib versus vehicle was determined using a two-tailed unpaired t test (Figs. 2D, 2E, 4F and 4G). Statistical significance of differences in blood counts of Tet2/NTG and Tet2/Stag2 mice in the presence and absence of treatment with talazoparib was determined using two-tailed unpaired t tests (Fig. 3D and 4C). Statistical significance of differences in *Stag2* and *Tet2* indel fraction in the bone marrow of Tet2/NTG and Tet2/Stag2 mice treated with talazoparib or vehicle was determined using two-tailed unpaired t tests (Fig. 4B). Statistical significance of differences in survival of *RAD21*-mutant PDX model treated with talazoparib or vehicle was determined using Kaplan Meier survival analysis (Fig. 4G). Statistical significance of differences in colocalizing coefficients of cohesin with PARP or RPA1 protein in *STAG2* wild type and mutant cells was determined using two-tailed unpaired t tests (Fig. 5G).

Study approval

All mouse experiments were conducted according to an IACUC approved protocol at the Broad Institute.

AUTHOR CONTRIBUTIONS

Z.T. and B.L.E. designed the research; Z.T., E.C., K.L., M.S., A.D.D., S.A.C., J.D., and B.L.E. supervised the research; Z.T., A.V., R.A.G, M.V., J.M.K.-B., A.H., C.C.L., E.M., C.H., J.E.H., M.D., K.D.P., S.K., and J.R. performed the research; Z.T., A.V., J.M.K.-B., A.H., C.C.L., E.M., C.H., M.D., K.D.P., J.R., E.C., S.V.V., M.S. and E.A.M. analyzed the data. Z.T. and B.L.E. wrote the manuscript.

ACKNOWLEDGEMENTS

We thank Drs. A. Spektor and A. Dall’Agnese for assistance with confocal microscopy, Drs. G. Cowley and S. Younger, and S. Pantel for technical advice, Y. Lee, and L. Ali for technical assistance, N. Abdenur for helpful discussions, and Dr. D. Neuberg for help with statistical analysis. This work was supported by the NIH (R01HL082945 and 479 P30CA006516), the Edward P. Evans Foundation, the Gabrielle’s Angel Foundation, The Leukemia & Lymphoma Society Scholar Award to B.L.E; National Human Genome Research Institute (HG003143 to J.D.); NIH (5K12CA087723-12 and 1K08HL140138-01), the Leukemia & Lymphoma Society Special Fellow Award (3363-13), ASCO Young Investigator Award, ASH Scholar award and ASH/EHA Translational Research in Hematology Award to Z.T.; and the NIH (T32GM007753) to S.K. B.L.E. and J.D are investigators of the Howard Hughes Medical Institute. This work was supported in part by grants from the National Cancer Institute (55) Clinical Proteomic Tumor Analysis Consortium grants NIH/NCI U24-CA210986 and NIH/NCI U01 CA214125 to S.A.C. We thank Dana-Farber/Harvard Cancer Center in Boston, MA, for the use of the Specialized Histopathology Core, which provided histology and immunohistochemistry service. Dana-Farber/Harvard Cancer Center is supported in part by an NCI Cancer Center Support Grant # NIH 5 P30 CA06516. A.D.D. consults for Lilly, EMD-Serono, Sierra and Cedilla Thepapeutics; S.A.C. is on the scientific advisory board for Kymera, Seer, PTM BioLabs, and a consultant for Biogen and Pfizer; B.L.E. has received research support from Celgene and Deerfield and consulting fees from Grail.

REFERENCES

1. Losada A. Cohesin in cancer: chromosome segregation and beyond. *Nat Rev Cancer*. 2014;14(6):389-93.
2. Lawrence MS, Stojanov P, Mermel CH, Robinson JT, Garraway LA, Golub TR, et al. Discovery and saturation analysis of cancer genes across 21 tumour types. *Nature*. 2014;505(7484):495-501.
3. Leiserson MD, Vandin F, Wu HT, Dobson JR, Eldridge JV, Thomas JL, et al. Pan-cancer network analysis identifies combinations of rare somatic mutations across pathways and protein complexes. *Nat Genet*. 2015;47(2):106-14.
4. Sperling AS, Gibson CJ, and Ebert BL. The genetics of myelodysplastic syndrome: from clonal haematopoiesis to secondary leukaemia. *Nat Rev Cancer*. 2017;17(1):5-19.
5. Papaemmanuil E, Gerstung M, Bullinger L, Gaidzik VI, Paschka P, Roberts ND, et al. Genomic Classification and Prognosis in Acute Myeloid Leukemia. *N Engl J Med*. 2016;374(23):2209-21.
6. Cancer Genome Atlas Research N. Genomic and epigenomic landscapes of adult de novo acute myeloid leukemia. *The New England journal of medicine*. 2013;368(22):2059-74.
7. Haferlach T, Nagata Y, Grossmann V, Okuno Y, Bacher U, Nagae G, et al. Landscape of genetic lesions in 944 patients with myelodysplastic syndromes. *Leukemia*. 2014;28(2):241-7.
8. Papaemmanuil E, Gerstung M, Malcovati L, Tauro S, Gundem G, Van Loo P, et al. Clinical and biological implications of driver mutations in myelodysplastic syndromes. *Blood*. 2013;122(22):3616-27; quiz 99.
9. Thota S, Viny AD, Makishima H, Spitzer B, Radivoyevitch T, Przychodzen B, et al. Genetic alterations of the cohesin complex genes in myeloid malignancies. *Blood*. 2014;124(11):1790-8.
10. Kon A, Shih LY, Minamino M, Sanada M, Shiraishi Y, Nagata Y, et al. Recurrent mutations in multiple components of the cohesin complex in myeloid neoplasms. *Nat Genet*. 2013;45(10):1232-7.
11. Welch JS, Ley TJ, Link DC, Miller CA, Larson DE, Koboldt DC, et al. The origin and evolution of mutations in acute myeloid leukemia. *Cell*. 2012;150(2):264-78.
12. Viny AD, Ott CJ, Spitzer B, Rivas M, Meydan C, Papalexis E, et al. Dose-dependent role of the cohesin complex in normal and malignant hematopoiesis. *J Exp Med*. 2015;212(11):1819-32.
13. Mazumdar C, Shen Y, Xavy S, Zhao F, Reinisch A, Li R, et al. Leukemia-Associated Cohesin Mutants Dominantly Enforce Stem Cell Programs and Impair Human Hematopoietic Progenitor Differentiation. *Cell Stem Cell*. 2015;17(6):675-88.
14. Mullenders J, Aranda-Orgilles B, Lhoumaud P, Keller M, Pae J, Wang K, et al. Cohesin loss alters adult hematopoietic stem cell homeostasis, leading to myeloproliferative neoplasms. *J Exp Med*. 2015;212(11):1833-50.
15. Viny AD, Bowman RL, Liu Y, Lavalley VP, Eisman SE, Xiao W, et al. Cohesin Members Stag1 and Stag2 Display Distinct Roles in Chromatin Accessibility and Topological Control of HSC Self-Renewal and Differentiation. *Cell Stem Cell*. 2019.

16. Holzmann J, Fuchs J, Pichler P, Peters JM, and Mechtler K. Lesson from the stoichiometry determination of the cohesin complex: a short protease mediated elution increases the recovery from cross-linked antibody-conjugated beads. *J Proteome Res.* 2011;10(2):780-9.
17. Lindsley RC, Mar BG, Mazzola E, Grauman PV, Shareef S, Allen SL, et al. Acute myeloid leukemia ontogeny is defined by distinct somatic mutations. *Blood.* 2015;125(9):1367-76.
18. Walker CJ, Eisfeld AK, Genutis LK, Bainazar M, Kohlschmidt J, Mrozek K, et al. No evidence for microsatellite instability in acute myeloid leukemia. *Leukemia.* 2017;31(6):1474-6.
19. Kojic A, Cuadrado A, De Koninck M, Gimenez-Llorente D, Rodriguez-Corsino M, Gomez-Lopez G, et al. Distinct roles of cohesin-SA1 and cohesin-SA2 in 3D chromosome organization. *Nat Struct Mol Biol.* 2018;25(6):496-504.
20. Wutz G, Ladurner R, St Hilaire BG, Stocsits RR, Nagasaka K, Pignard B, et al. ESCO1 and CTCF enable formation of long chromatin loops by protecting cohesin(STAG1) from WAPL. *Elife.* 2020;9.
21. Casa V, Moronta Gines M, Gade Gusmao E, Slotman JA, Zirkel A, Josipovic N, et al. Redundant and specific roles of cohesin STAG subunits in chromatin looping and transcriptional control. *Genome Res.* 2020;30(4):515-27.
22. Ochi Y, Kon A, Sakata T, Nakagawa MM, Nakazawa N, Kakuta M, et al. Combined Cohesin-RUNX1 Deficiency Synergistically Perturbs Chromatin Looping and Causes Myelodysplastic Syndromes. *Cancer Discov.* 2020;10(6):836-53.
23. Doench JG, Fusi N, Sullender M, Hegde M, Vaimberg EW, Donovan KF, et al. Optimized sgRNA design to maximize activity and minimize off-target effects of CRISPR-Cas9. *Nat Biotechnol.* 2016;34(2):184-91.
24. Benedetti L, Cereda M, Monteverde L, Desai N, and Ciccarelli FD. Synthetic lethal interaction between the tumour suppressor STAG2 and its paralog STAG1. *Oncotarget.* 2017;8(23):37619-32.
25. van der Lelij P, Lieb S, Jude J, Wutz G, Santos CP, Falkenberg K, et al. Synthetic lethality between the cohesin subunits STAG1 and STAG2 in diverse cancer contexts. *Elife.* 2017;6.
26. Eisfeld AK, Mrozek K, Kohlschmidt J, Nicolet D, Orwick S, Walker CJ, et al. The mutational oncoprint of recurrent cytogenetic abnormalities in adult patients with de novo acute myeloid leukemia. *Leukemia.* 2017;31(10):2211-8.
27. Heidinger-Pauli JM, Mert O, Davenport C, Guacci V, and Koshland D. Systematic reduction of cohesin differentially affects chromosome segregation, condensation, and DNA repair. *Curr Biol.* 2010;20(10):957-63.
28. Terret ME, Sherwood R, Rahman S, Qin J, and Jallepalli PV. Cohesin acetylation speeds the replication fork. *Nature.* 2009;462(7270):231-4.
29. Tittel-Elmer M, Lengronne A, Davidson MB, Bacal J, Francois P, Hohl M, et al. Cohesin association to replication sites depends on rad50 and promotes fork restart. *Mol Cell.* 2012;48(1):98-108.
30. Wu N, and Yu H. The Smc complexes in DNA damage response. *Cell Biosci.* 2012;2:5.

31. Mondal G, Stevers M, Goode B, Ashworth A, and Solomon DA. A requirement for STAG2 in replication fork progression creates a targetable synthetic lethality in cohesin-mutant cancers. *Nat Commun.* 2019;10(1):1686.
32. Benedict B, van Schie JJM, Oostra AB, Balk JA, Wolthuis RMF, Riele HT, et al. WAPL-Dependent Repair of Damaged DNA Replication Forks Underlies Oncogene-Induced Loss of Sister Chromatid Cohesion. *Dev Cell.* 2020;52(6):683-98 e7.
33. Nieminuszczy J, Schwab RA, and Niedzwiedz W. The DNA fibre technique - tracking helicases at work. *Methods.* 2016;108:92-8.
34. Watrin E, and Peters JM. The cohesin complex is required for the DNA damage-induced G2/M checkpoint in mammalian cells. *EMBO J.* 2009;28(17):2625-35.
35. Kong X, Ball AR, Jr., Pham HX, Zeng W, Chen HY, Schmiesing JA, et al. Distinct functions of human cohesin-SA1 and cohesin-SA2 in double-strand break repair. *Mol Cell Biol.* 2014;34(4):685-98.
36. McLellan JL, O'Neil NJ, Barrett I, Ferree E, van Pel DM, Ushey K, et al. Synthetic lethality of cohesins with PARPs and replication fork mediators. *PLoS Genet.* 2012;8(3):e1002574.
37. Song WJ, Sullivan MG, Legare RD, Hutchings S, Tan X, Kufrin D, et al. Haploinsufficiency of CBFA2 causes familial thrombocytopenia with propensity to develop acute myelogenous leukaemia. *Nat Genet.* 1999;23(2):166-75.
38. Guillou E, Ibarra A, Coulon V, Casado-Vela J, Rico D, Casal I, et al. Cohesin organizes chromatin loops at DNA replication factories. *Genes Dev.* 2010;24(24):2812-22.
39. Lieberman-Aiden E, van Berkum NL, Williams L, Imakaev M, Ragoczy T, Telling A, et al. Comprehensive mapping of long-range interactions reveals folding principles of the human genome. *Science.* 2009;326(5950):289-93.
40. Belaghzal H, Dekker J, and Gibcus JH. Hi-C 2.0: An optimized Hi-C procedure for high-resolution genome-wide mapping of chromosome conformation. *Methods.* 2017;123:56-65.
41. Nora EP, Goloborodko A, Valton AL, Gibcus JH, Uebersohn A, Abdennur N, et al. Targeted Degradation of CTCF Decouples Local Insulation of Chromosome Domains from Genomic Compartmentalization. *Cell.* 2017;169(5):930-44 e22.
42. Crane E, Bian Q, McCord RP, Lajoie BR, Wheeler BS, Ralston EJ, et al. Condensin-driven remodelling of X chromosome topology during dosage compensation. *Nature.* 2015;523(7559):240-4.
43. Rao SS, Huntley MH, Durand NC, Stamenova EK, Bochkov ID, Robinson JT, et al. A 3D map of the human genome at kilobase resolution reveals principles of chromatin looping. *Cell.* 2014;159(7):1665-80.
44. Gassler J, Brandao HB, Imakaev M, Flyamer IM, Ladstatter S, Bickmore WA, et al. A mechanism of cohesin-dependent loop extrusion organizes zygotic genome architecture. *EMBO J.* 2017;36(24):3600-18.
45. Mufti GJ EE, Popat R, Mattison R, Menne T, Azar J, et al. . Results of a phase 1 study of BMN 673, a potent and specific PARP-1/2 inhibitor, in patients with advanced hematological malignancies. *Haematologica.* 2014;99:33-4.

46. Bailey ML, O'Neil NJ, van Pel DM, Solomon DA, Waldman T, and Hieter P. Glioblastoma cells containing mutations in the cohesin component STAG2 are sensitive to PARP inhibition. *Mol Cancer Ther.* 2014;13(3):724-32.
47. Tothova Z, Krill-Burger JM, Popova KD, Landers CC, Sievers QL, Yudovich D, et al. Multiplex CRISPR/Cas9-Based Genome Editing in Human Hematopoietic Stem Cells Models Clonal Hematopoiesis and Myeloid Neoplasia. *Cell Stem Cell.* 2017;21(4):547-55 e8.
48. Muvarak NE, Chowdhury K, Xia L, Robert C, Choi EY, Cai Y, et al. Enhancing the Cytotoxic Effects of PARP Inhibitors with DNA Demethylating Agents - A Potential Therapy for Cancer. *Cancer cell.* 2016;30(4):637-50.
49. Fritz C, Portwood SM, Przespolewski A, and Wang ES. PARP goes the weasel! Emerging role of PARP inhibitors in acute leukemias. *Blood Rev.* 2020:100696.
50. Rao SSP, Huang SC, Glenn St Hilaire B, Engreitz JM, Perez EM, Kieffer-Kwon KR, et al. Cohesin Loss Eliminates All Loop Domains. *Cell.* 2017;171(2):305-20 e24.
51. Schwarzer W. Two independent modes of chromatin organization revealed by cohesin removal. *Nature.* 2017.
52. Dekker J, and Mirny L. The 3D Genome as Moderator of Chromosomal Communication. *Cell.* 2016;164(6):1110-21.
53. Hnisz D, Weintraub AS, Day DS, Valton AL, Bak RO, Li CH, et al. Activation of proto-oncogenes by disruption of chromosome neighborhoods. *Science.* 2016;351(6280):1454-8.
54. Flavahan WA, Drier Y, Liao BB, Gillespie SM, Venteicher AS, Stemmer-Rachamimov AO, et al. Insulator dysfunction and oncogene activation in IDH mutant gliomas. *Nature.* 2016;529(7584):110-4.
55. Zhang X, Choi PS, Francis JM, Imielinski M, Watanabe H, Cherniack AD, et al. Identification of focally amplified lineage-specific super-enhancers in human epithelial cancers. *Nat Genet.* 2016;48(2):176-82.
56. Kluk MJ, Lindsley RC, Aster JC, Lindeman NI, Szeto D, Hall D, et al. Validation and Implementation of a Custom Next-Generation Sequencing Clinical Assay for Hematologic Malignancies. *J Mol Diagn.* 2016;18(4):507-15.
57. Della Porta MG, Galli A, Bacigalupo A, Zibellini S, Bernardi M, Rizzo E, et al. Clinical Effects of Driver Somatic Mutations on the Outcomes of Patients With Myelodysplastic Syndromes Treated With Allogeneic Hematopoietic Stem-Cell Transplantation. *J Clin Oncol.* 2016.

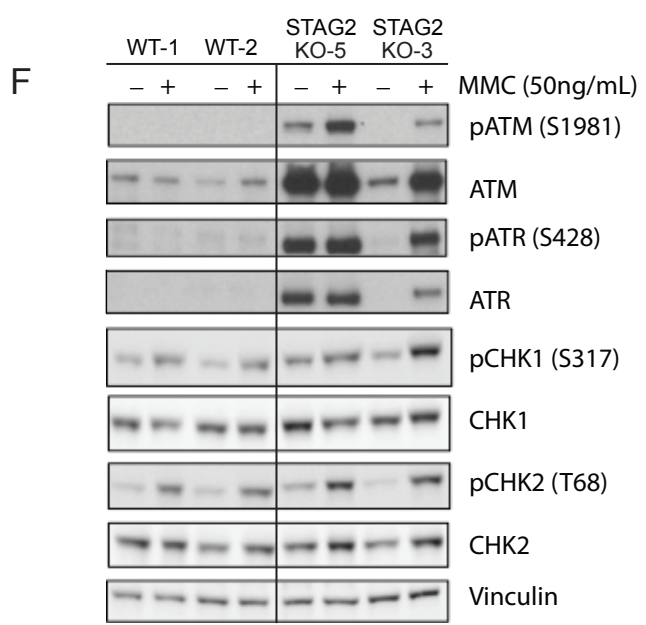
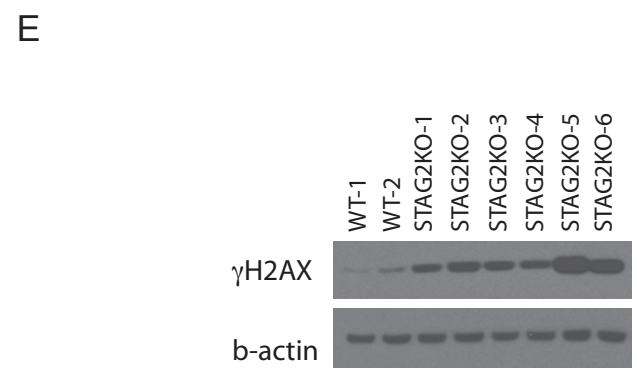
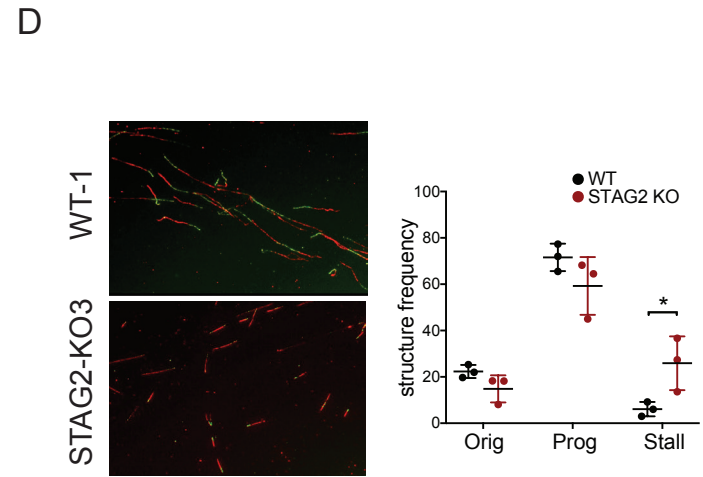
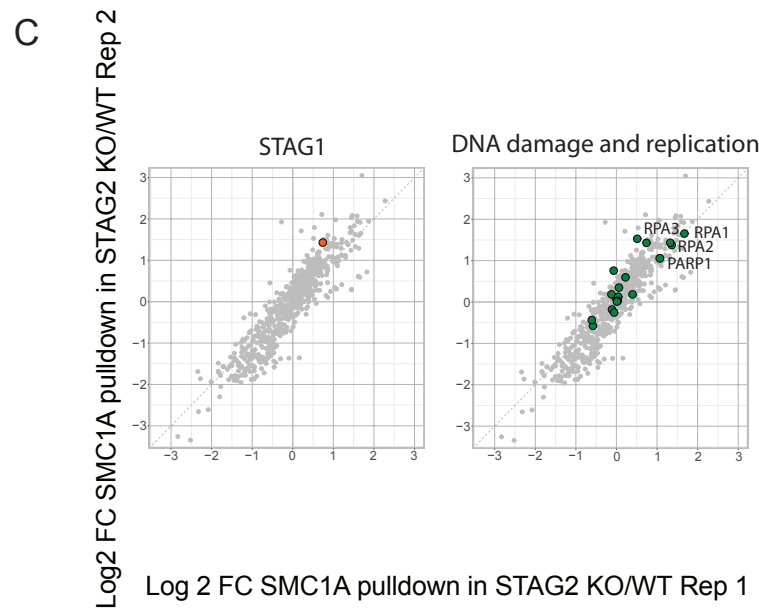
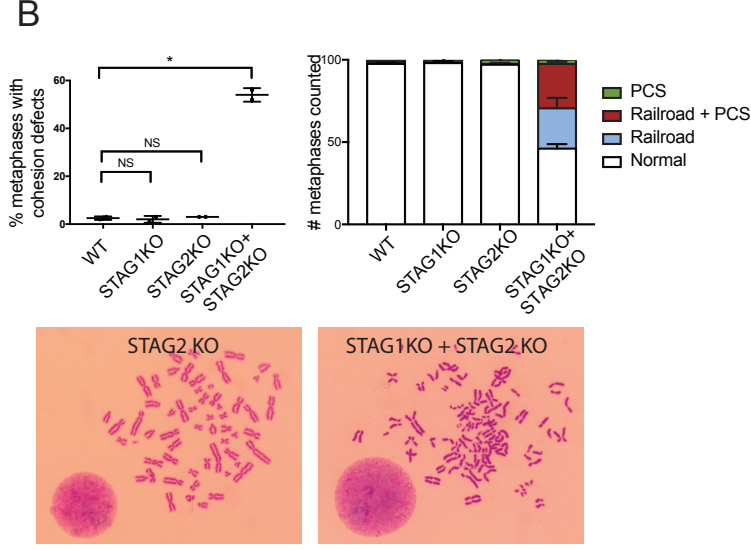
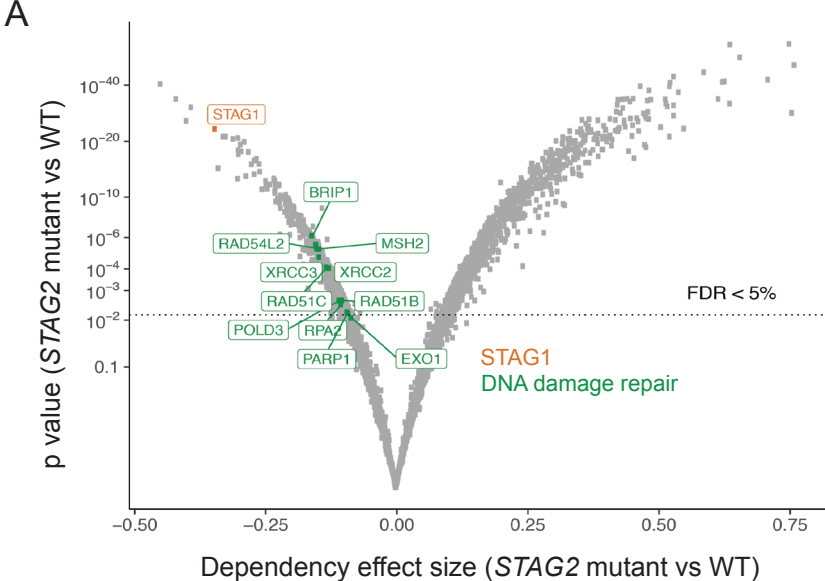


Figure 1.

Figure 1: Identification of DNA replication and damage repair as a dependency in *STAG2*-mutant cells

A, Volcano plot depicting differential dependencies in *STAG2*-mutant versus WT cells. Composite data for 5 *STAG2*-mutant cell lines (U937 *STAG2*-KO2, *STAG2*-KO3, KOC5, KOD5C, KOG8B) and 6 *STAG2*-WT cell lines (U937 WT-1, WT-2, NCB1, NCB12, NCB2A, NCC4) is shown. Respective sets of genes representing dependency in *STAG2*-mutant over WT cells with FDR<5% are shown in color.

B, Metaphase chromosome spreads and cohesion defect analysis in WT, *STAG1* KO, *STAG2* KO and double *STAG1 STAG2* KO cells. Mean +/-SD is shown for two independent biological replicates of *STAG2* wild type (U937 WT-1, WT-2) and *STAG2* knockout cells (U937 *STAG2*-KO3, *STAG2*-KO4) transduced with *STAG1* or control sgRNAs. 100 metaphase spreads were scored for each sample in a blinded fashion. * denotes p<0.0001 (one-way ANOVA). PCS = premature centromere separation. Railroad = railroad chromosomes.

C, Log2 fold change (FC) of protein enrichment after SMC1A IP-MS in WT and *STAG2*-knockout (KO) cells. Rep1 and Rep2 correspond to different mutant clones. Proteins belonging DNA damage repair and replication gene set are highlighted in green. Enrichment p value was determined using a one-tailed Fisher's exact test (p(DNA damage and replication)=0.024). U937 WT-1, WT-2, *STAG2*-KO5 and *STAG2*-KO6 were used in this experiment.

D, Representative images depicting replication structures of single combed DNA molecules labeled with IdU (red) and CldU (green) in WT and *STAG2*-knockout cells. Quantification of replication origin firing (Orig), progressing replication forks (Prog) and stalled replication forks (Stall) in WT and *STAG2*-mutant cells. Data from 3 WT (U937 WT-1, WT-2, WT-3) and 3 *STAG2*-knockout (U937 *STAG2*-KO2, *STAG2*-KO3, *STAG2*-KO4) cell lines combined. p<0.05 (unpaired Student t-test).

E, Assessment of dsDNA breaks in WT and *STAG2*-mutant cells using Western blotting for γ -H2Ax. Representative images shown. U937 WT-1, WT-2, *STAG2* KO-1, *STAG2* KO-2, *STAG2* KO-3, *STAG2* KO-4, *STAG2* KO-5 and *STAG2* KO-6 were used in this experiment. β -actin was used as a loading control.

F, Western blotting for DNA damage checkpoint proteins ATM, pATM, ATR, pATR, CHK1, pCHK1, CHK2, and pCHK2 in WT and *STAG2*-mutant cells in the presence and absence of mitomycin C. Vinculin was used as a loading control.

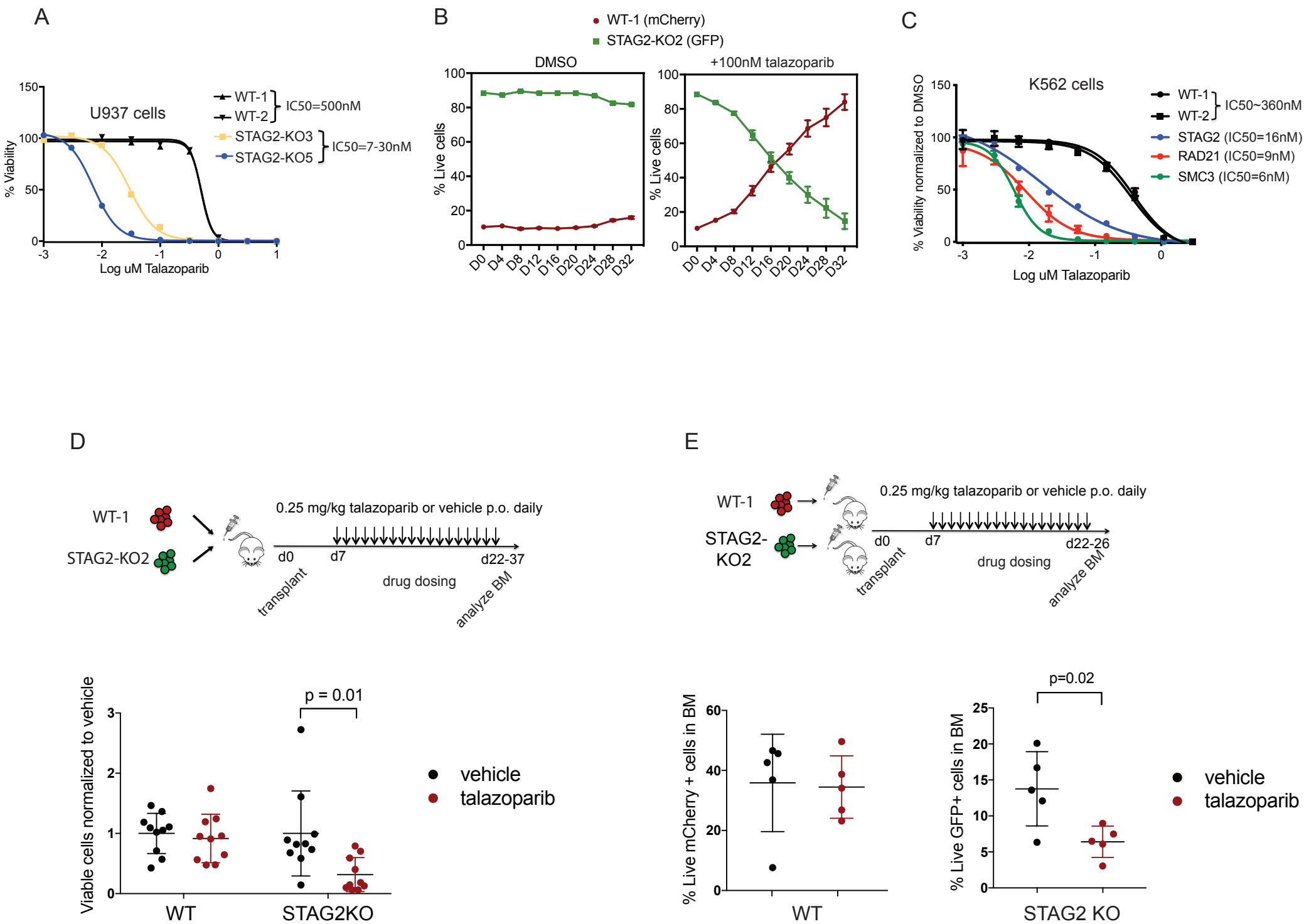


Figure 2.

Figure 2: STAG2-mutant AML cell lines are more sensitive to PARP inhibition *in vitro* and *in vivo*

A, Drug dose response curves of WT and STAG2-mutant U937 cell lines treated with the PARP inhibitor talazoparib. U937 WT-1, WT-2, STAG2 KO-3, and STAG2 KO-5 cells were used for this experiment. IC_{50} (WT) = 500nM, IC_{50} (STAG2 KO) = 7-30nM on Day 12 of treatment. Error bars represent SD of measurements of triplicate technical replicates.

B, Competition assay with WT (U937 WT-1-mCherry) and STAG2-knockout (U937 STAG2-KO2-GFP) cells mixed in 1:10 ratio in the presence of DMSO or talazoparib (100nM) *in vitro*. % Live GFP+ or mCherry+ cells were determined using flow cytometry. Error bars represent SD of measurements of triplicate technical replicates.

C, Drug dose response curves of WT and STAG2-, SMC3-, and RAD21-mutant K562 clones treated with talazoparib. IC_{50} (WT) = 360nM, IC_{50} (STAG2 KO) = 16nM, IC_{50} (SMC3 het) = 6nM, and IC_{50} (RAD21 het) = 9nM on Day 12 of treatment. Error bars represent SD of measurements of three technical replicates.

D, Schematic of the *in vivo* drug treatment of WT and STAG2KO xenografts. WT (U937 WT-1-mCherry) and STAG2-knockout (U937 STAG2-KO2-GFP) cells were mixed 1:1 and transplanted into NSGS recipients and dosed with talazoparib or vehicle by oral gavage at 0.25mg/kg once a day, starting on day 7 after transplantation. Leukemia burden in mice treated with talazoparib or vehicle was assessed in the bone marrow of animals at the time of sacrifice. % Live GFP+ or mCherry+ cells were determined using flow cytometry. Mean +/- SD is shown. $p=0.01$ (Student t-test). $n=10$ mice per group.

E, Schematic of the *in vivo* drug treatment of WT and STAG2 KO xenografts. WT (U937 WT-1 mCherry) or STAG2 KO (U937 STAG2-KO2-GFP) cells were transplanted into NSGS recipients and dosed with talazoparib or vehicle by oral gavage at 0.25mg/kg once a day starting on day 7 after transplantation. Leukemia burden in mice treated with talazoparib or vehicle was assessed in the bone marrow of animals at the time of sacrifice. % Live GFP+ or mCherry+ cells were determined using flow cytometry. Mean +/- SD is shown. $p=0.02$ (Student t-test). $n=5$ mice per group.

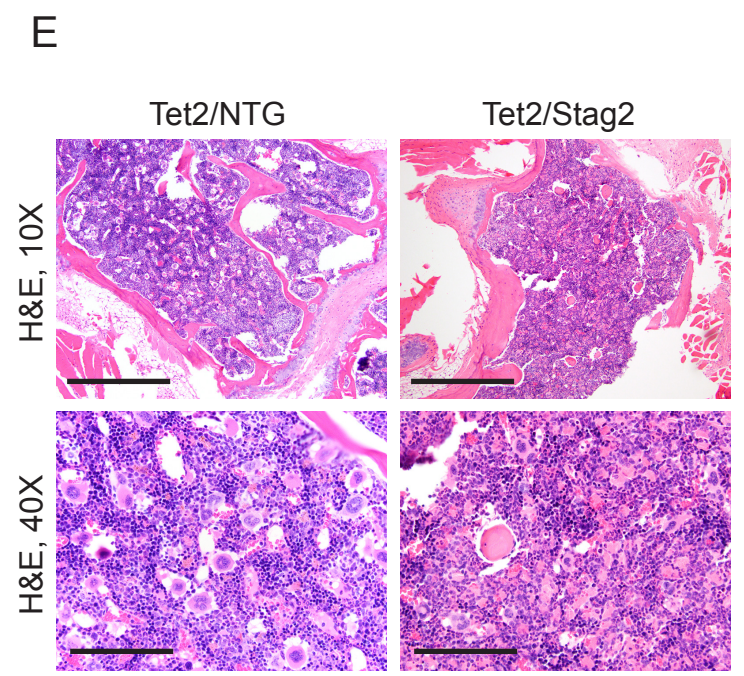
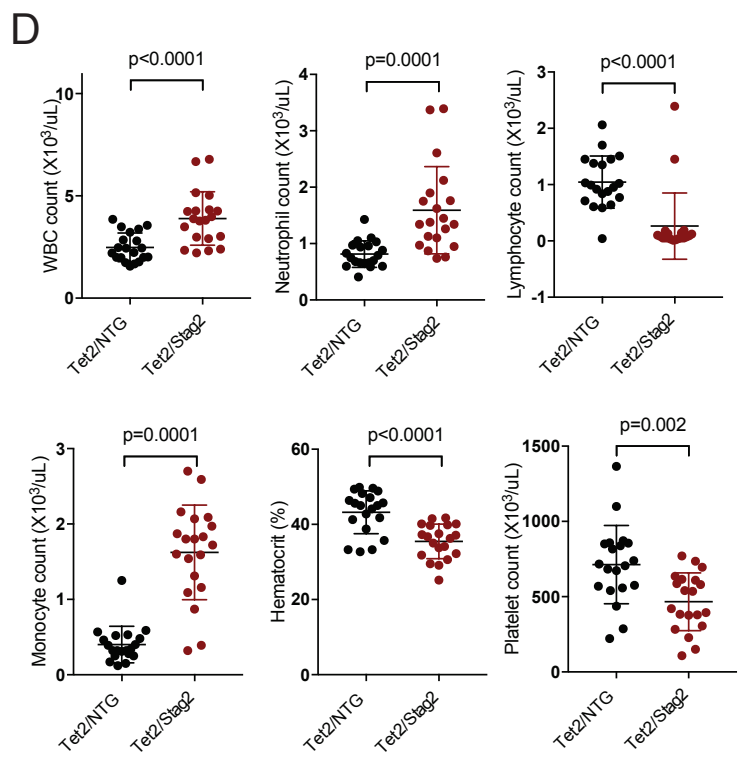
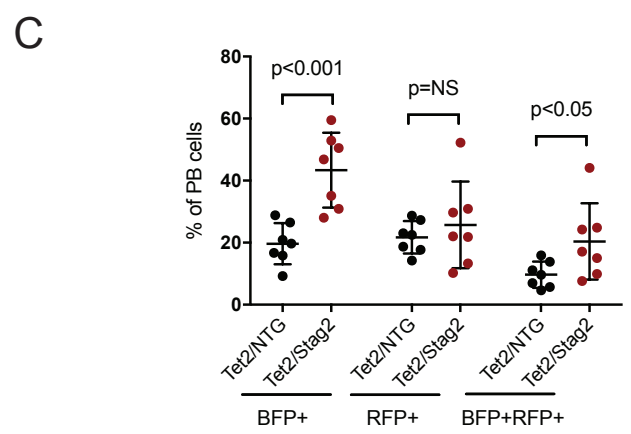
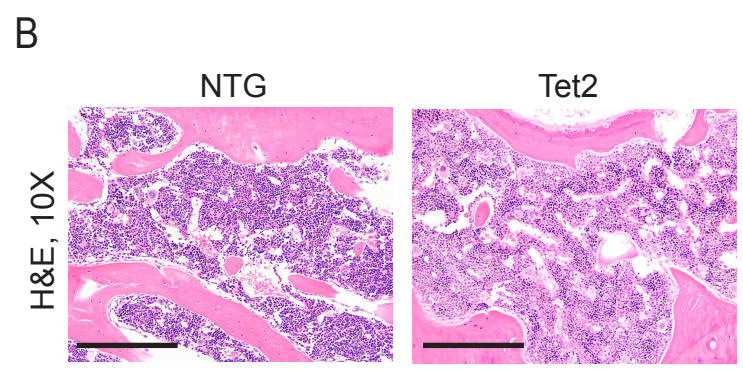
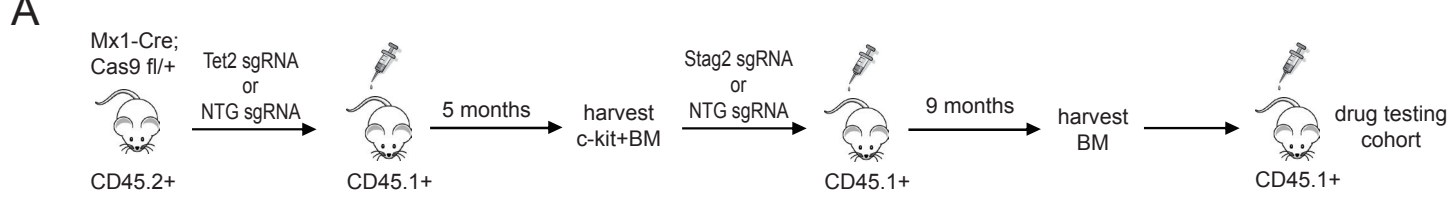


Figure 3.

Figure 3: Development of primary models of cohesin-mutant MDS

A, Schematic of the sequential bone marrow transplant used to generate *Tet2/Stag2*-mutant models of myeloid disease.

B, Morphologic evaluation of bone marrow section of mice injected with NTG and *Tet2*-mutant cells. H&E staining, 10X magnification. No appreciable differences were observed. Scale bar =0.5mm.

C, Flow cytometry analysis of peripheral blood samples of mice sequentially transplanted with *Tet2*/NTG and *Tet2/Stag2* 3 months after transplantation. BFP reporter is linked to expression of sgRNA targeting *Stag2*, and RFP reporter is linked to expression of sgRNA targeting *Tet2*. Expansion of BFP+ and BFP+RFP+ cells in *Tet2/Stag2* animals. n=7 per arm. Mean +/-SD shown.

D, Absolute white blood cell (WBC) count, neutrophil count, lymphocyte count, monocyte count, hematocrit and platelet count were measured in *Tet2*/NTG and *Tet2/Stag2*-mutant mice 12 weeks after bone marrow transplantation. Mean +/- SD is shown. p values were determined using the Student t-test. n=20 mice per group.

E, Morphologic evaluation of bone marrow of a representative *Tet2*/NTG and *Tet2/Stag2*-mutant mouse shows a decrease in megakaryocytes and increased erythrophagocytosis in *Tet2/Stag2*-mutant mice. Images were stained using H&E and imaged at 10X (scale bar = 0.5mm) and 40X (scale bar = 0.125mm) magnification.

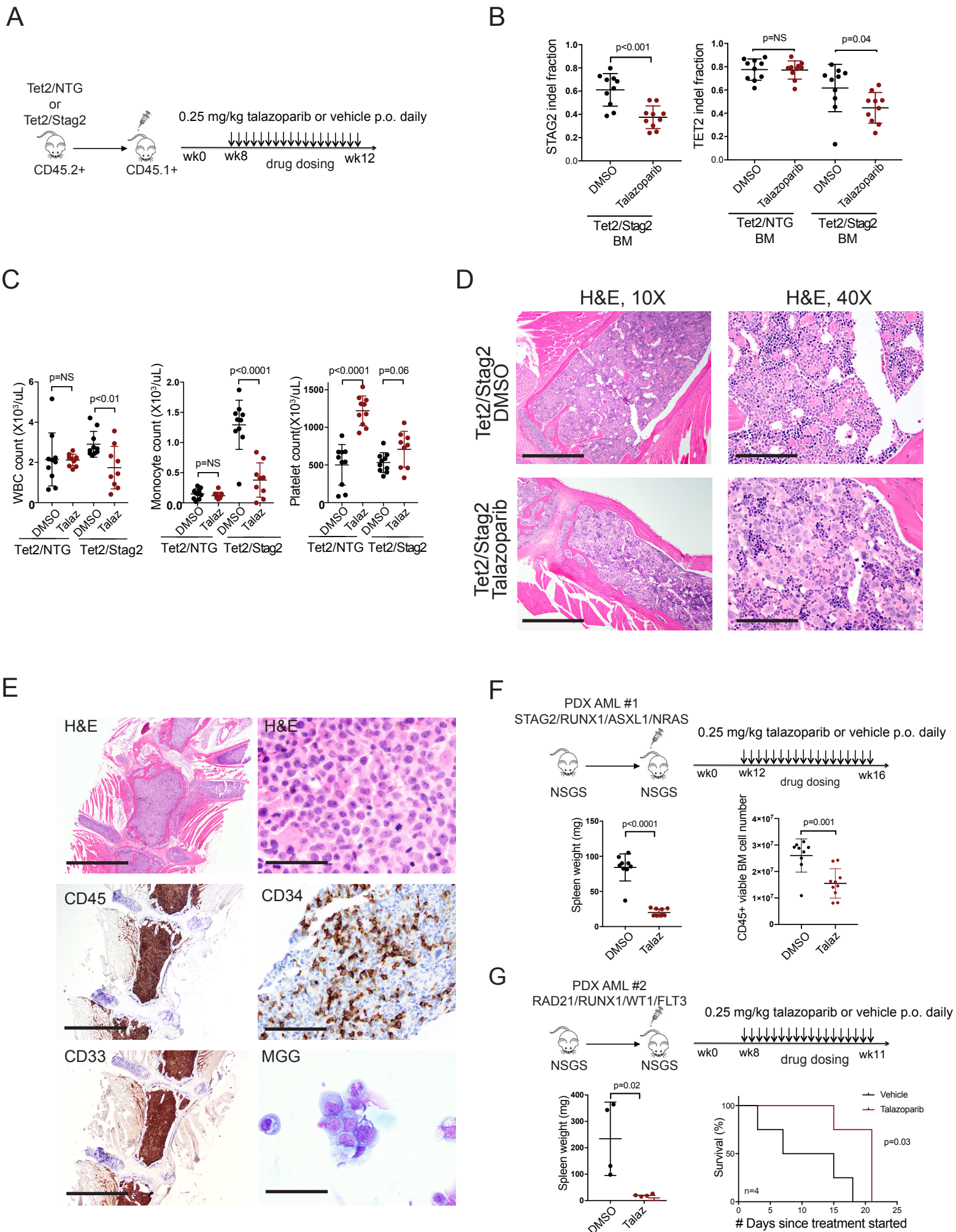


Figure 4.

Figure 4. Talazoparib treatment preferentially depletes cohesin-mutant clones in primary mouse and human cell *in vivo* models of cohesin-mutant myeloid diseases

A, Schematic of the *in vivo* drug treatment of *Tet2*/NTG and *Tet2*/*Stag2*-mutant mice with talazoparib. CD45.2+*Tet2*/NTG or *Tet2*/*Stag2*-mutant cells were transplanted into CD45.1+ recipients and dosed with talazoparib or vehicle by oral gavage at 0.25mg/kg once a day starting 8 weeks after transplantation.

B, Bone marrow analysis of *Stag2* and *Tet2* indel fraction by NGS demonstrates a genotype-specific response to talazoparib treatment in *Tet2*/*Stag2* but not *Tet2*/NTG-mutant clones. Mean +/- SD is shown. p values were determined using the Student t-test. n=10 mice per group.

C, Complete blood count analysis shows normalization of the white blood cell (WBC), monocyte and platelet counts in talazoparib treated *Tet2*/*Stag2* animals. Mean +/- SD is shown. p values were determined using the Student t-test. n=10 mice per group.

D, Morphologic evaluation of bone marrow of representative *Tet2*/*Stag2*-mutant mice treated with talazoparib or DMSO shows an increased megakaryocyte number and persistent erythrophagocytosis in *Tet2*/*Stag2*-mutant mice treated with talazoparib. Images were stained using H&E and imaged at 10X (scale bar = 0.5mm) and 40X (scale bar = 0.125mm) magnification.

E, Generation of a *STAG2*-mutant AML PDX model model in NSGS mice. Staining with H&E, Modified Giemsa May-Grunwald (MGG) and immunohistochemistry (IHC) show expansion of immature CD45+CD34+CD33+ myeloid blasts in the bone marrow. Images were taken using 10x (scale bar = 0.5mm) and 100X magnification (scale bar = 0.05mm). NGS sequencing confirmed presence of a single *STAG2*-mutant clone with the following VAFs: *STAG2* p.R1012* (0.92), *RUNX1* p.R320* (0.43), *ASXL1* p. p.G642fs*(0.48) and *NRAS* p.G13D(0.45).

F, Schematic of the *in vivo* drug treatment of *STAG2*-mutant AML PDX model. *STAG2*/*RUNX1*/*ASXL1*/*NRAS*-mutant PDX cells were transplanted into NSGS recipients and dosed with talazoparib or vehicle by oral gavage at 0.25mg/kg once a day starting 12 weeks after transplantation. Mice were sacrificed after completing 4 weeks of treatment and showed a decrease in spleen size and human CD45+ bone marrow disease burden in the talazoparib-treated arm. Mean +/- SD is shown. p values were determined using the Student t-test. n=9-10 mice per group.

G, Schematic of the *in vivo* drug treatment of *RAD21*-mutant AML PDX model. *RAD21*/*RUNX1*/*WT1*/*FLT3*-mutant PDX cells were transplanted into NSGS recipients and dosed with talazoparib or vehicle by oral gavage at 0.25mg/kg once a day starting 8 weeks after transplantation. Treatment with talazoparib led to a decrease in spleen size and improved overall survival. Mean +/- SD is shown. p values were determined using the Student t-test and Kaplan-Meier survival analysis. n=4 mice per group.

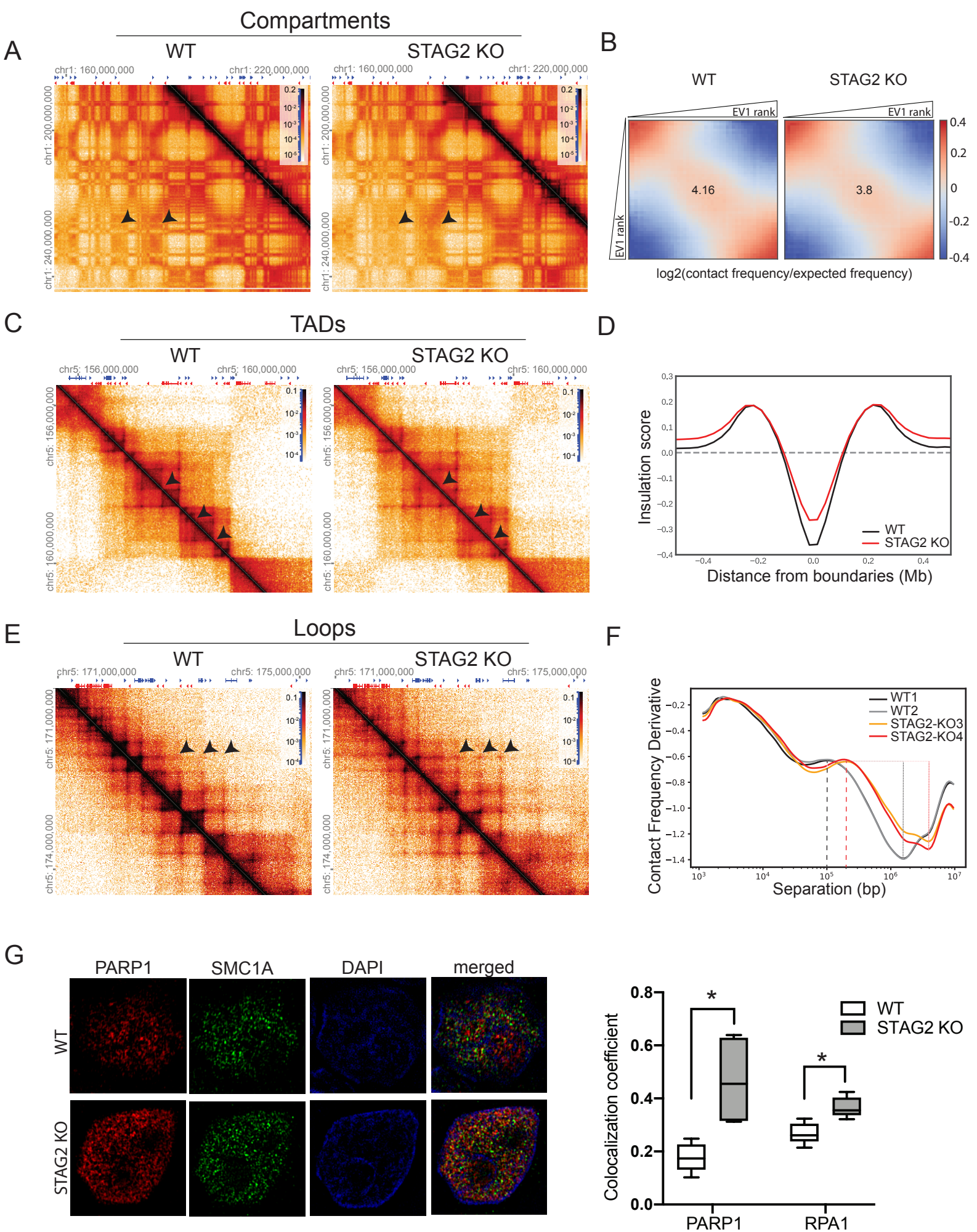


Figure 5.

Figure 5: STAG2 loss disrupts normal chromatin folding and association with DNA replication and damage repair proteins

A Hi-C interaction maps for chromosome 1 binned at 100kb in WT vs STAG2-KO cells to visualize compartments. Arrow heads depict examples of weakened compartments.

B, Saddle plots of Hi-C data binned at 100kb resolution normalized by genomic distance. Saddle plots were generated using the PC1 from the sample. The numbers at the center of the heatmaps indicate compartment strength calculated as the ratio of $(AA+BB)/(AB+BA)$ using the values from a 10 bin X 10 bin square starting from the corner. The saddle plot demonstrates global weakening of compartments in STAG2-KO cells. Heatmaps were generated using Hi-glass from pooled reads from 2 independent WT (U937 WT-1, WT-2) and STAG2-knockout (U937 STAG2-KO3, STAG2-KO4) cell lines.

C, Hi-C interaction maps for a genomic region in chromosome 5 binned at 25kb in WT vs STAG2-KO cells to visualize TADs. Heatmaps were generated using Hi-glass from pooled reads from 2 independent WT (U937 WT-1, WT-2) and STAG2-knockout (U937 STAG2-KO3, STAG2-KO4) cell lines. Arrow heads depict examples of loss of TAD insulation.

D, Insulation score as defined by (42) as a function of distance from TAD boundaries demonstrates global weakening of insulation at TAD boundaries.

E, Hi-C interaction maps for a genomic region in chromosome 5 binned at 10kb in WT vs STAG2-KO cells to visualize loops. Arrow heads depict examples of gain of longer loops.

F, Relationship between interaction frequency (P) and genomic distance (s) is used to estimate the average loop size and density in STAG2 KO and WT cells. The position of a local maximum in the derivative of $P(s)$ represents the average loop size, while the difference between the local maximum and the valley directly to the right of it is a measure for the loop density (loops per kb; (44)). Extruded loops are longer in STAG2 KO cells compared to WT cells (represented by dashed lines, U937 WT1, WT2 ~100 kb; U937 STAG2-KO3, KO4 ~ 200kb) and the density of loops is reduced in STAG2 KO cells (represented by dotted lines).

G, Super-resolution structured illumination microscopy of co-localization of SMC1A with PARP1 in WT (U937 WT-1, WT-2) and STAG2-knockout (U937 STAG2-KO-3, STAG2-KO5) cells. Fluorescence signal displayed alone and merged with the nuclear Hoechst stain. Quantification of co-localization of SMC1A with PARP1 or RPA1 in WT (U937 WT-1) and STAG2-knockout (U937 STAG2-KO5) cells using Manders colocalization coefficient. Box and whiskers represent mean +/- Tukey. $p < 0.0001$, unpaired Student t-test.